JOURNAL OF GEOPHYSICAL RESEARCH, VOL. 112, D21103, doi:10.1029/2006JD008368, 2007

Observation and analysis of a large amplitude mountain wave event over the Antarctic peninsula

M. Joan Alexander[1] and Hector Teitelbaum[2]

Received 20 December 2006; revised 27 April 2007; accepted 31 July 2007; published 7 November 2007.

[1] We use measurements from the Atmospheric Infrared Sounder (AIRS) on the AQUA satellite to observe the 3-dimensional structure of a gravity wave event over the Antarctic peninsula, and determine the horizontal and vertical wavelengths, propagation direction, and temperature amplitude, and from these we estimate wave momentum flux. Using theoretical knowledge of the weighting functions and radiative transfer for AIRS radiance measurements at temperature sensitive channels in the infrared, we derive a method of estimating wave temperature amplitude directly from the radiance measurements. Comparison of the radiance-based temperature amplitudes to the temperature amplitude in AIRS retrieved temperature fields shows close agreement. Because the radiances have 3-times better horizontal resolution than the retrievals, our analysis suggests we can routinely observe important geophysical properties of waves with horizontal wavelengths as short as 80 km using AIRS radiances. We further analyze a nearly identical wave event appearing in the European Centre for Medium Range Forecasts (ECMWF) temperature and wind fields from both assimilation and forecast data. Analysis of the ECMWF data and nearby radiosonde wind profiles allows the interpretation as a mountain wave event forced by flow over the topography of the Antarctic peninsula.

Citation: Alexander, M. J., and H. Teitelbaum (2007), Observation and analysis of a large amplitude mountain wave event over the Antarctic peninsula, *J. Geophys. Res.*, *112*, D21103, doi:10.1029/2006JD008368.

1. Introduction

[2] Mountain waves have important effects on the high-latitude tropospheric and stratospheric circulation and chemistry [*Palmer et al.*, 1986; *McFarlane*, 1987; *Bacmeister*, 1993; *Carslaw et al.*, 1998; *Dörnbrack et al.*, 2001; *Fueglistaler et al.*, 2003; *Eckermann et al.*, 2006a]. The Antarctic peninsula in particular is a singular formidable obstacle to the circumpolar southern ocean winds, and a known mountain wave source region [*Bacmeister et al.*, 1994, 1990; *Höpfner et al.*, 2006].

[3] Mountain waves have been observed via satellite with infrared [*Eckermann and Preusse*, 1999; *Preusse et al.*, 2002] and microwave [*Jiang et al.*, 2002, 2004; *Wu and Jiang*, 2002] limb scanning instruments. In a case study using Cryogenic Infrared Spectrometers and Telescopes for the Atmosphere (CRISTA) measurements, *Eckermann and Preusse* [1999] were able to infer both the horizontal and vertical wavelengths and the temperature amplitude of an Andean mountain wave event, and estimate the wave momentum flux and mean-flow forcing. It is difficult to determine all of these detailed properties for wave events observed from satellite. Most other satellite studies in the literature have instead reported averaged temperature variances, and mountain wave sources were then sometimes inferred on the basis of proximity to topography. (See above references and also *Tsuda et al.* [2000] and *Wu* [2004].) Most recently, mountain waves have been observed by nadir viewing imaging instruments in the infrared [*Alexand and Barnet*, 2007] and microwave [*Eckermann et al.*, 2006b].

[4] We describe a mountain wave event observed in three dimensions from Atmospheric Infrared Sounder (AIRS) satellite radiance measurements and retrieved temperatures. We also examine temperature and wind fields from the European Centre for Medium-Range Weather Forecasts (ECMWF), where the wave event appears with very similar properties. We will examine both AIRS retrieved temperature (Level 2 data) as well as raw radiance (Level 1B data) perturbations converted to temperature. The raw radiances have three times better horizontal resolution than the AIRS retrieved temperatures. AIRS temperature-sensitive channels have weighting functions with vertical widths ~12 km. This limits the detection of waves to those with vertical wavelengths longer than 12 km [*Alexander and Barnet*, 2007]. For waves with wavelengths longer than this limit, the temperature retrieval algorithm should sharpen the vertical structure by synthesizing measurements from many AIRS channels that peak at different altitudes. For waves, this sharpening should result in a larger amplitude wave in the temperature retrievals than in measurements from individual channels, although this has not previously been examined in any detail.

[1] NorthWest Research Associates, Colorado Research Associates Div., Boulder, Colorado, USA.
[2] Laboratoire de Meteorologie Dynamique, Paris, France.

0148-0227/07/2006JD008368$09.00

[5] We will describe the observed event and describe similarities and differences between the event seen in AIRS radiances, AIRS temperature retrievals, and ECMWF temperatures. The results allow the interpretation of this as a mountain wave event with an approximate duration of 24 h. The horizontal wavelength of the event is observed to be ~300 km in the stratosphere. This large-scale wave event is also resolved in both ECMWF and AIRS retrieved temperature fields. Further examination of AIRS radiances shows small horizontal scale waves that dominate the radiance perturbations at altitudes below 30 km, that are absent in the ECMWF and AIRS retrievals because of insufficient horizontal resolution.

2. Data Description

2.1. AIRS CO_2 Channel Radiances and Temperature Retrievals

[6] The Atmospheric Infrared Sounder (AIRS) is a multispectral imaging instrument on the Aqua satellite launched in 2002. AIRS acquires radiance image swaths with 90 cross-track pixels and a total width of 1600 km [*Aumann et al.*, 2003]. Gravity waves are detected by AIRS via the temperature perturbations they induce in the atmosphere. Here we examine both AIRS radiances at temperature-sensitive channels as well as temperature retrievals. The temperature retrievals combine information from both AIRS and AMSU-A (Advanced Microwave Sounding Unit-A). Clouds have a significant effect on AIRS radiances but have smaller effect on AMSU-A microwave radiances [*Susskind et al.*, 2003, 2006]. The AMSU-A radiances are used to produce a ''cloud-cleared'' AIRS radiance product prior to the temperature retrieval. The AIRS footprint at nadir is 13.5 km. A 3 × 3 array of AIRS footprints falls into a single AMSU-A footprint [*Aumann et al.*, 2003]. The AIRS cloud-cleared radiance and temperature products therefore have horizontal resolution reduced by a factor of 3 in each dimension giving 40.5 km resolution at nadir. Some smaller-scale waves are therefore eliminated in the retrieval process and can only be studied using AIRS radiances. We therefore look for waves in the raw radiance data (Level 1B), which have the highest resolution, but we also use the temperature retrievals (Level 2) when possible.

[7] AIRS radiance measurements include channels that span the two temperature sounding CO_2 bands near 15 μm and 4.2 μm. For this work, we use measurements from 22 of these channels spanning altitudes ~8–43 km (pressure levels from 320 to 2 hPa). The AIRS weighting functions reference pressure surfaces, but for the purpose of wave analysis, we convert the vertical pressure grid to log-pressure altitude using a reference pressure of 1000 hPa and a scale height of 7 km. Throughout the paper, ''altitude'' refers to this log-pressure altitude.

[8] We examine channels in the 15 μm band and 4.2 μm band for our analysis of gravity wave three-dimensional (3-d) structure. The radiance weighting functions are broad in the vertical, roughly approximating a Gaussian with full-width-at-half-maximum (FWHM) of ~12 km. The weighting function vertical profiles describe the smearing of information in the vertical associated with the radiance measurements. Because of this, wave oscillations with adjacent positive and negative perturbations will be invisible to AIRS if the vertical wavelength is shorter than 12 km. At longer vertical wavelengths, the measured amplitude will be attenuated relative to the true wave amplitude depending on the vertical wavelength of the wave as described by *Alexander and Barnet* [2007]. The temperature retrieval process includes measurements from AIRS channels with adjacent overlapping weighting functions that can be used to remove some of this vertical smearing effect. The retrieval process is therefore expected to realistically increase the amplitudes of attenuated waves with vertical wavelengths >12 km, however waves with short vertical wavelengths (<12 km) cannot be recovered.

[9] The weighting functions for the AIRS channels chosen for our analysis do not intersect the ground, but the lower altitude channels sometimes intersect clouds. The wave radiance perturbations are weak enough that cloud signals easily overwhelm the wave perturbations, so we discard the lowest channels that intersect clouds from the analysis. For the winter high latitude case described here, we can use channels that peak at 9.9 km (247 hPa) and above. Each of these AIRS channels has a unique radiance response to a given temperature perturbation given by

$$\frac{R'}{R} = \frac{T'_{1B}}{T}\left(\frac{hc\nu}{kT}\right), \tag{1}$$

where R'/R is the fractional radiance perturbation, h is Planck's constant, c is the speed of light, ν is wave number associated with each channel, k is the Boltzmann constant, T'_{1B} is the temperature perturbation, and T is background temperature. We give the temperature perturbation T'_{1B} the subscript '1B' to note its derivation directly from the Level 1B radiances, and to distinguish it from the Level 2 temperature retrievals. With (1) for each of our selected channels, we can convert a map of radiance perturbations to a map of temperature perturbations.

[10] To fully exploit the AIRS data, we also compute a vertical grid of radiance perturbation maps, which retain the full horizontal resolution of the Level 1B measurements. We choose 11 channels in each of the 15 μm and 4.2 μm bands that span altitudes from the troposphere to ~43 km altitude. The kernel functions for these channels are estimated as by *Alexander and Barnet* [2007, Equation [3]]. These kernel functions are interpolated to constant vertical resolution of 1-km, then normalized by their sum to give approximate weighting functions, which are plotted in Figure 1. Channels with kernel functions that peak at adjacent altitudes are binned using a noise-dependent weight factor. Each channel has differing noise characteristics given by the noise-equivalent ΔT (NEΔT). *Aumann et al.* [2000] describe NEΔT as a function of channel number for the AIRS measurements. Using these noise estimates, we compute a vertically gridded temperature product. A weighted average of channels in each vertical bin is computed using a weighting equal to $(\mathrm{NE}\Delta T)^{-1}$ to construct the 3-d gridded fields.

[11] The NEΔT of the individual channels ranges 0.14–0.19 K for 4.2 μm channels (below 23 km), and 0.39–0.43 K for the 15 μm channels. From these we compute a 3.33-km resolution altitude grid, averaging maps from adjacent altitudes using a 1/NEΔT weight factor. The altitude binning results in noise estimates that range 0.07–0.11 K below 23 km and 0.18–0.30 K above.

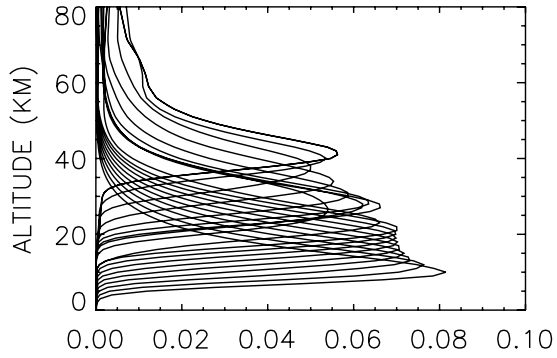

Figure 1. Weighting functions for 11 channels with ν = 667.5–670.1 cm^{-1} (peaking above 23 km) and 11 channels with ν = 2376–2386 cm^{-1} (peaking below 23 km). These channels are used to create the vertically gridded radiance fields.

2.2. ECMWF Analysis and Forecast Fields

[12] We also analyze European Centre for Medium-Range Forecasts (ECMWF) wind and temperature fields. The ECMWF fields are computed at T_L511 spectral resolution and with 60 sigma-pressure hybrid coordinate levels in the vertical between the surface and 0.1 hPa. We will show results from both ECMWF analysis fields and forecast fields. The case we examine occurs in September 2003, and at this time AIRS data were not assimilated in the ECMWF product. The ECMWF fields are available every 3 h: At 00, 06, 12, and 18 UT the fields are assimilations, while fields at 03, 09, 15, and 21 UT are 3 or 9 hour forecast fields initialized at either 00 or 12 UT.

2.3. Operational Radiosonde

[13] We also examine operational radiosonde winds from Marambio located at 57°W longitude, 64°S latitude. These data are used in the ECMWF assimilation. The profiles we examine extend from the surface to 6 hPa pressure.

3. Results

3.1. Atmospheric Infrared Sounder

[14] Figure 2 shows maps of radiance perturbations from channels at four altitudes spanning 10–43 km converted to temperature perturbations using (1) and a background temperature derived from the horizontal mean of the temperature retrieval. As done by *Alexander and Barnet* [2007], radiance perturbations are derived for each cross-track scan by subtraction of a fourth-order polynomial fit to remove limb-brightening effects.

[15] *Alexander and Barnet* [2007] describe a wavelet analysis method that determines amplitude, horizontal wavelength, and propagation direction as functions of

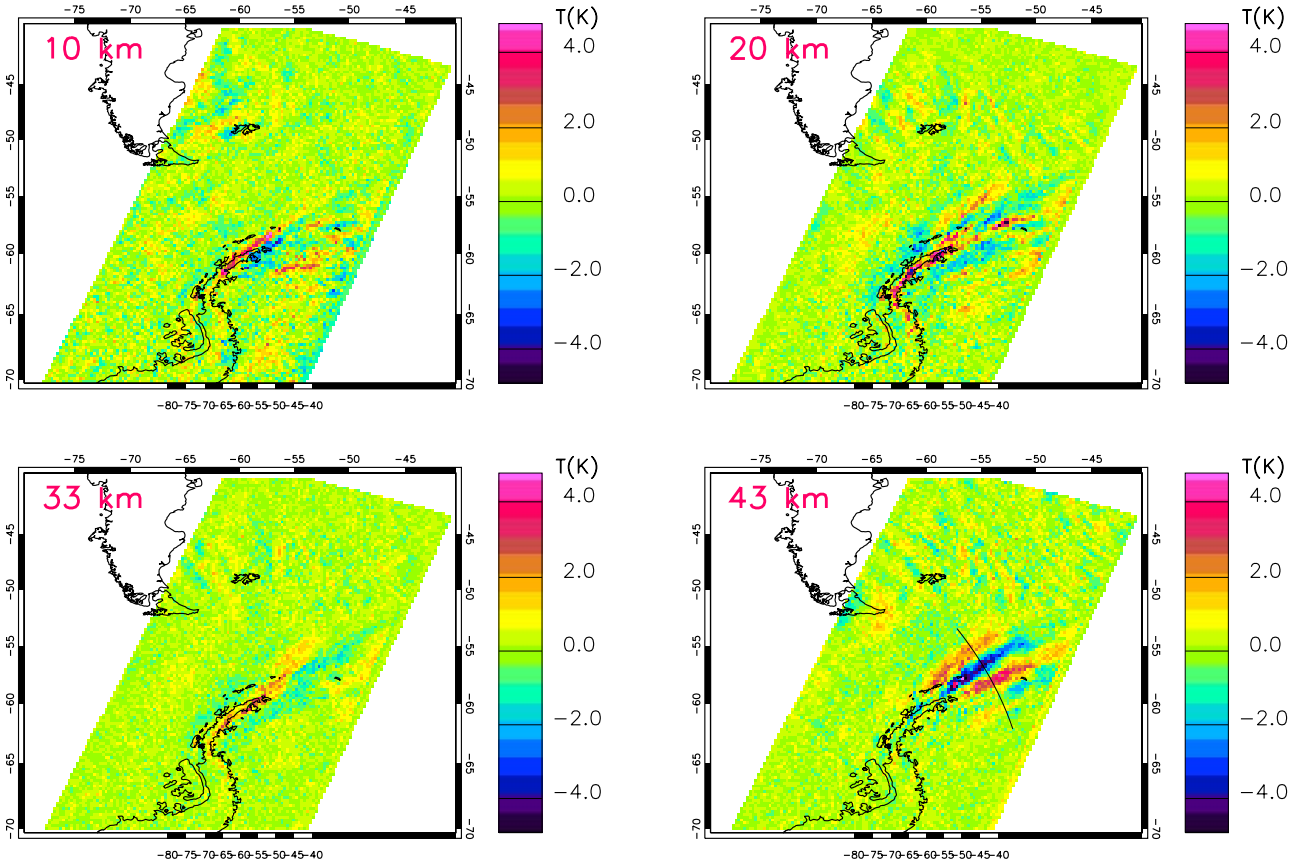

Figure 2. Maps of the wave event at four altitudes in AIRS vertically gridded radiances plotted as T_{1B} on 10 September 2003 at ~04:20Z. The estimated noise levels are 0.07 K (10 km), 0.07 K (20 km), 0.29 K (33 km), and 0.30 K (43 km). The black line in the last panel shows the location of cross sections shown in subsequent figures.

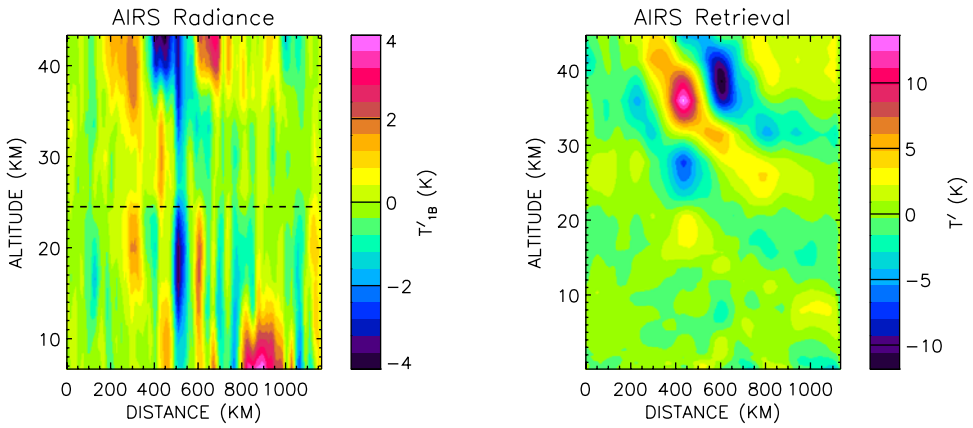

Figure 3. (a) Radiance perturbation cross-section from channels with weighting functions peaking at altitudes ranging from 8 to 43 km. These have been converted to a temperature scale using (1), and vertically gridded as described in the text. (b) Identical cross-section of AIRS retrieved temperature perturbations, showing sharpened vertical structure, but an absence of the short horizontal scale wave features below 30 km. The location of the cross-sections is shown in Figure 2.

latitude and longitude for wave events observed in the AIRS radiances. In the stratosphere above 30 km the wavelet analysis gives a horizontal wavelength of 300 km for this event with a propagation direction of 41 degrees north of west. Shorter horizontal-scale wave features are also seen at altitudes below 30 km, and these shorter horizontal wavelength waves dominate the radiance perturbations below 25 km. Figure 3 shows cross-sections along the black line overplotted on Figure 2 through the center of the large amplitude wave event. The horizontal axis runs from northwest to southeast along the cross-sections. Figure 3a shows the vertically gridded radiances. Above the dashed line, the radiances are from 15 μm channels while below they are from 4.2 μm channels. Figure 3b shows the cross-section of AMSU-AIRS version 4 temperature retrieval. Perturbations are derived at each altitude by subtraction of a parabolic fit to the horizontal temperature variations.

[16] As previously mentioned, the AIRS temperatures are only retrieved at a horizontal resolution three times coarser than the radiances. The process of retrieving temperature from AIRS radiances can sharpen vertical variations seen in the raw radiances, including the vertical phase variations in waves with vertical wavelengths longer than 12 km. The wave in the stratosphere above 25 km that has large horizontal wavelength is clearly resolved in the retrieved temperatures and can also be seen in the gridded radiances. The amplitude is 12 K in the retrieval and 4 K in the radiances. The vertical wavelength can also be estimated at 20 km from both the retrieval and the radiances. The fact that the amplitude is three times larger in the retrieved temperatures than the temperature amplitude T'_{1B} estimated directly from the radiances can be understood with the radiance amplitude attenuation factor for a 20-km vertical wavelength wave shown by *Alexander and Barnet* [2007, Figure 4]. The radiance temperature amplitude T'_{1B} = 4 K divided by the attenuation factor (0.3) is approximately equal to the temperature amplitude from the retrieval T'. This agreement between the wave properties derived from the gridded radiances and the temperature retrievals indicates that we may be able to infer three-dimensional properties of waves directly from the higher resolution radiances.

[17] The AIRS temperature retrieval algorithm was not designed with small-scale waves in mind. This case of a well resolved wave with horizontal wavelength 300 km and vertical wavelength 20 km shows the temperature retrieval does a good job of retrieving the correct wave amplitude and wavelengths probably because the wave feature is well-resolved by both AIRS and AMSU-A [*Eckermann and Wu*, 2006]. There is also shorter horizontal wavelength structure that appears in the higher-resolution radiances that is absent in the retrieved temperatures. The finer-scale structure is most prominent in the 4.2 μm channels below 25 km. The apparent discontinuity in some of these features at 25 km altitude leads us to suspect that the shapes of the approximate weighting functions for these lower altitude channels are inaccurate. In particular, we suspect these channels have weighting functions with more complex shape and deeper vertical extent than shown in Figure 1 (Lars Hoffmann, personal communication). We therefore defer the interpretation of these structures below 25 km in Figure 3a to future work, and tentatively conclude here that the 15 μm channels above 25 km can be used to study 3-d wave structure at the full resolution of the level 1B radiances.

3.2. ECMWF Temperature and Wind Fields

[18] Figure 4 shows a cross-section of ECMWF temperature perturbations at the same location as those in Figure 3. The perturbations are computed as deviations from a parabolic fit along the cross-section at each altitude. The ECMWF temperatures in Figure 4 are from the assimilation at 0600 UT, approximately 1.5 h after the AIRS data were acquired. The wave in the assimilation has very similar properties to the wave in the AIRS retrieved temperature field (Figure 3b). The vertical resolution of the ECMWF fields varies with height, but is similar to the ~3 km resolution of AIRS temperature retrievals in the middle stratosphere. The T_L511 resolution gives equivalent horizontal resolution of ~33 km at these latitudes. This is approximately 1/9 the horizontal wavelength of the wave

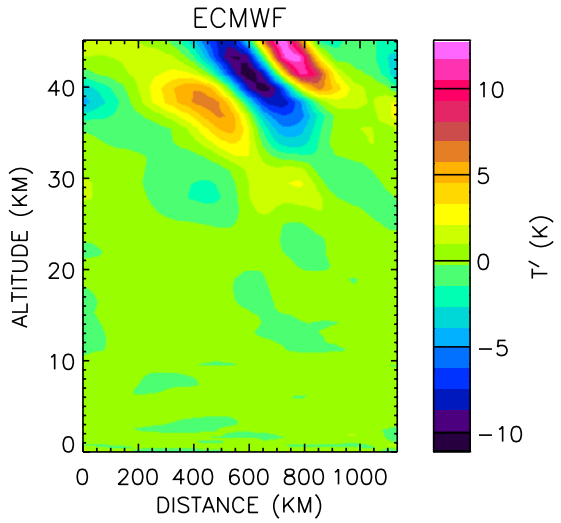

Figure 4. Vertical cross section of ECMWF temperature perturbations along the line shown in Figure 2.

seen by AIRS above 30 km. The smaller-scale structure seen in AIRS radiances is not well resolved in ECMWF.

[19] Figure 5 shows the horizontal structure of the wave event in the horizontal wind divergence field at two altitudes, 5 km and 40 km. In this plan view, the waves are most clearly separated from background variations in the divergence field because the background winds are geostrophic and therefore non-divergent. (In contrast, the definition of background temperature variations requires the selection of an ad hoc horizontal scale to distinguish waves from other gradients.) Similar to the AIRS observations (Figure 2), a shift in position of the wave event toward the north with increasing altitude is seen here, and the horizontal structure is very similar in AIRS and ECMWF. The wave event is clearly related to the topography of the Antarctic peninsula.

[20] Unlike the AIRS data, which sample the location of the wave event only every 12 h, we can examine the time evolution of the wave event in the ECMWF fields. Figure 6 shows the horizontal wind divergence at 30-km altitude at three times 00, 03, and 06 UT. Data from 00 UT and 06 UT are from the ECMWF assimilation, while data from 03 UT are from the ECMWF forecast initialized at 00UT. The same wave event appears in both assimilation and forecast fields, and it is stationary in time. The event first appears in ECMWF at 12 UT on 9 September and persists for over a day, through 18 UT on 10 September, and weakening thereafter. The wave is stationary above the Antarctic peninsula from at least 18 UT on 9 September until at least 12 UT on 10 September, supporting the inference of an orographic origin for this wave event.

[21] The speed and direction of the winds from the ECMWF assimilation at 06 UT on 10 September are shown in Figure 7 at the first sigma-p hybrid level. The near-surface winds blow perpendicular to the ridge line along the Antarctic peninsula at 15 m s^{-1}, further supporting the orographic origin of the wave, and suggesting this is a mountain wave event forced by flow over the peninsula topography, which rises to 1800 m altitude at 64°S latitude.

3.3. Radiosonde Winds

[22] A mountain wave is apparent in the wind profile from a radiosonde launched at 20 UT on 10 September 2003 from the Antarctic peninsula at Marambio. Earlier soundings are not available from this site. Figure 8 shows linearly detrended wind profiles of two perpendicular wind compo-

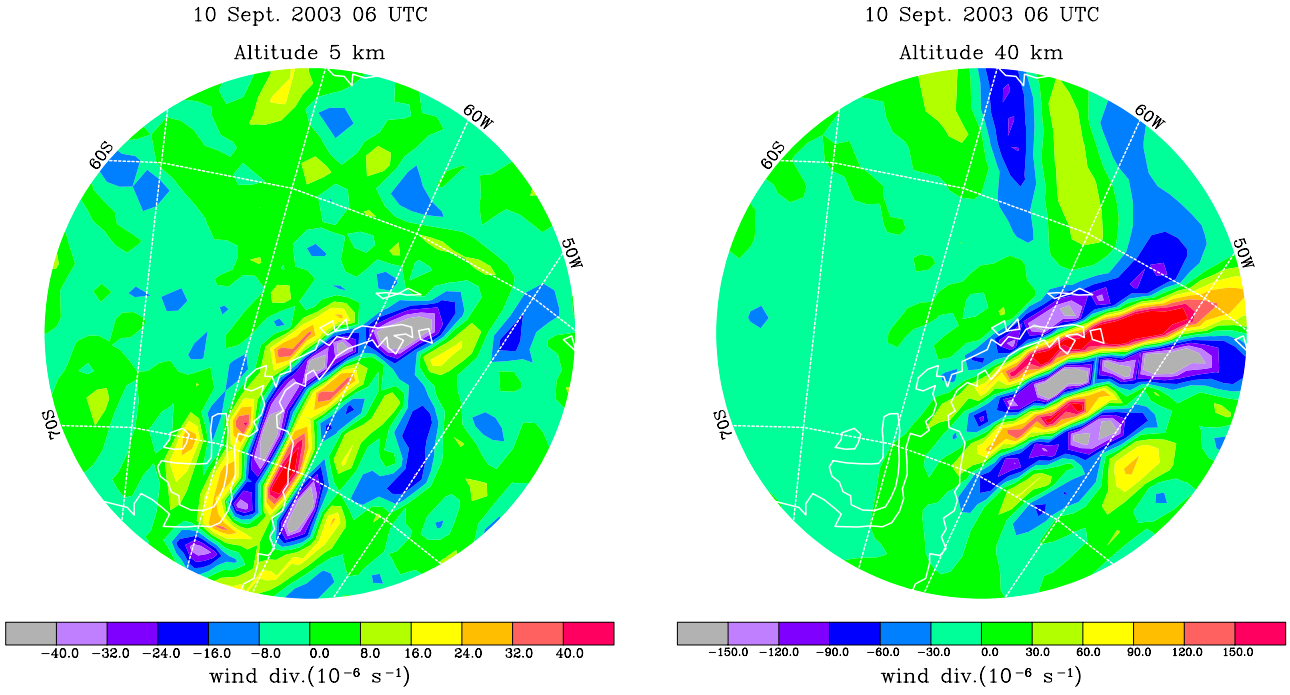

Figure 5. ECMWF horizontal wind divergence multiplied by a factor 10^6 at 06 UT at (a) z = 5 km and (b) z = 40 km.

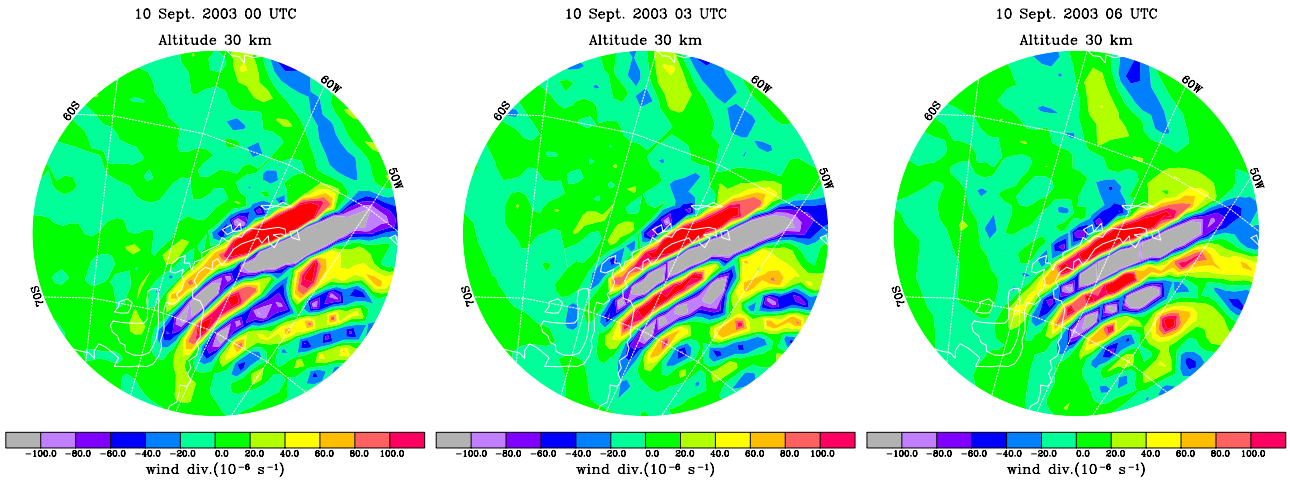

Figure 6. ECMWF horizontal wind divergence multiplied by a factor 10^6 at 30 km at times (a) 00 UT, (b) 03 UT, and (c) 06 UT.

nents u_R (solid) and v_R (dashed) in a coordinate system rotated by 80 degrees clockwise from the cardinal directions. This angle was chosen to maximize the linear correlation coefficient between u_R and v_R. When u_R and v_R are in phase, a linearly polarized gravity wave is propagating along the 45-degree axis line in the new rotated coordinate system. Knowledge of the southeastward surface wind direction breaks the 180° ambiguity in this determination of the propagation direction, giving a direction of 35° ± 5° north of west, an angle very similar to the AIRS-derived propagation direction of 41° north of west in the stratosphere. For reference, Figure 9 shows profiles of the zonal and meridional wind derived from the radiosonde superimposed on ECMWF wind components (both in the unrotated coordinate frame).

4. Discussion

[23] The interpretation of the wave event observed in the AIRS satellite data as a mountain wave is supported by: (i) the coincident stationary wave seen in ECMWF, (ii) by the observation of 15 m s^{-1} surface wind with direction perpendicular to the Antarctic Peninsula ridge, (iii) by the observed orientation of wave phase fronts perpendicular to surface wind, and (iv) by radiosonde observation of a wave propagating in the troposphere in the same direction. The vertical wavelength in the stratosphere inferred from AIRS also agrees with the linear theoretical vertical wavelength for stationary gravity wave propagating through the ECMWF winds. Figure 10 shows theoretical vertical wavelength versus height from the gravity wave dispersion relation $\lambda_Z = 2\pi U/N$, where N is the buoyancy frequency and U is the ECMWF wind along the axis of observed wave propagation. The 20-km wavelength observed by AIRS in the stratosphere above 30 km compares well to this theoretical mountain wave wavelength. (Note that the wave intrinsic frequency here is ten times larger than the Coriolis parameter, so rotational correction terms in the dispersion relation can be neglected [*Dörnbrack et al.*, 1999].) The above evidence strongly supports the origin of the wave event seen in ECMWF and AIRS as a mountain wave.

[24] The horizontal morphology of the wave event is similar in the AIRS radiances (Figure 2) and in the ECMWF fields. In particular, in both AIRS and ECMWF, the wave perturbations extend further north over the ocean at the higher altitudes, but are more closely tied to the peninsula topography at the lower altitudes. In the AIRS radiances at 43 km (Figure 2), the wave pattern disappears directly above the topography and is seen only over ocean. The reason for this disappearance is likely due to vertical wavelength limits associated with the AIRS observational filter. Since waves with vertical wavelengths shorter than

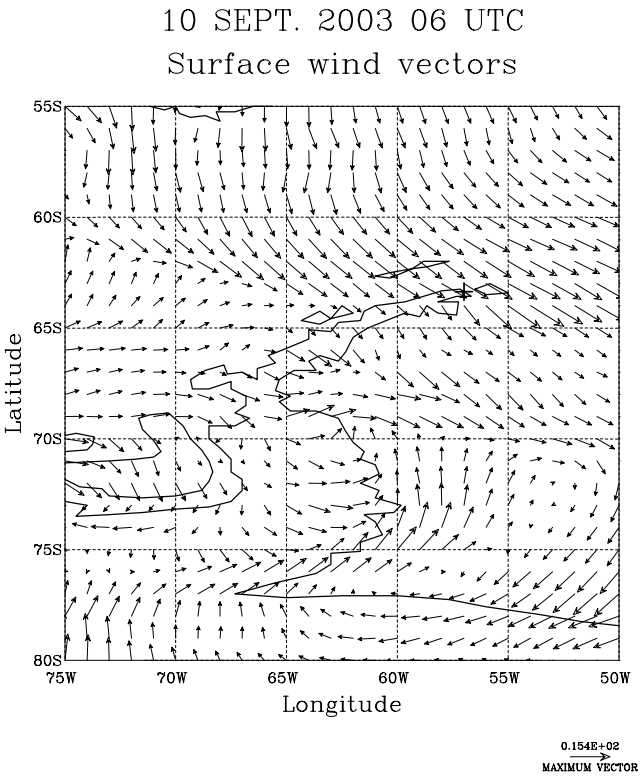

Figure 7. ECMWF near-surface wind vectors and the continental outline. Maximum length vector is 15.4 m s^{-1}.

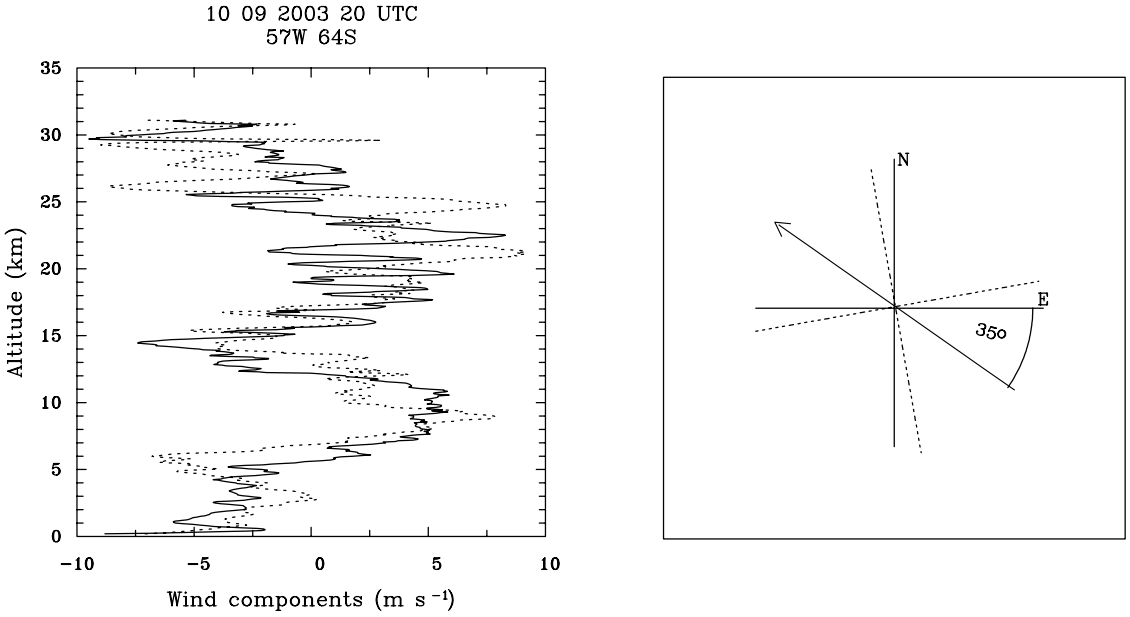

Figure 8. Linearly detrended horizontal wind components u'_R (solid) and v'_R (dotted) in m s^{-1}, where the subscript R denotes the rotated coordinate frame shown in the right panel as dashed lines. The angle of rotation was determined by finding the maximum correlation between the two wind components. This determines the propagation direction of the gravity wave to be in the direction given by the solid arrow.

12 km are invisible to AIRS, and since the vertical wavelength of a mountain wave is directly proportional to the wind speed in the direction of wave propagation, horizontal variations in the winds can give rise to differing visibility of the wave pattern in the horizontal cross section. Wind speeds must exceed 40 m s^{-1} in the direction of wave propagation for mountain waves to have vertical wavelengths longer than 12 km, the visibility limit for AIRS.

[25] In particular, we can compare winds off the coast at 60°S, 50°W to winds over the peninsula at 65°S, 60°W. Off the coast, winds opposite to the direction of wave propagation vary from 57–92 m s^{-1} between 30–43 km, while over the peninsula they vary between 40–52 m s^{-1} in this height range, and are only 40 m s^{-1} at 40-km altitude. The mountain wave is therefore likely to have too small a vertical wavelength to be visible to AIRS directly over the peninsula.

[26] Our 3-d observation of the wave horizontal and vertical wavelengths and temperature amplitude allow a direct estimate of the vertical flux of horizontal momentum of the event in the stratosphere. Parameterizations of mountain wave drag in general circulation models (GCMs) include a tuning parameter that sets the mountain wave momentum flux [e.g., *Mcfarlane*, 1987]. Observations such as ours may be used to better constrain these tuning parameters for future GCM applications. The magnitude of the momentum flux (M) can be estimated using linear wave theory [*Ern et al.*, 2004] and the medium frequency approximation [*Fritts and Alexander*, 2003] as,

$$M = \bar{\rho}\frac{k}{m}\left(\frac{g}{N}\right)^2\overline{\left(\frac{T'}{\bar{T}}\right)^2}, \qquad (2)$$

where $\bar{\rho}$ is the density, k and m are the horizontal and vertical wave numbers, and g is the gravitational acceleration. Using our observed wave properties at 40 km altitude, with temperature amplitudes corrected for the smearing effect of the vertical weighting functions, we estimate $M\sim$ 0.14 Pa, and the direction of the vector flux is north-

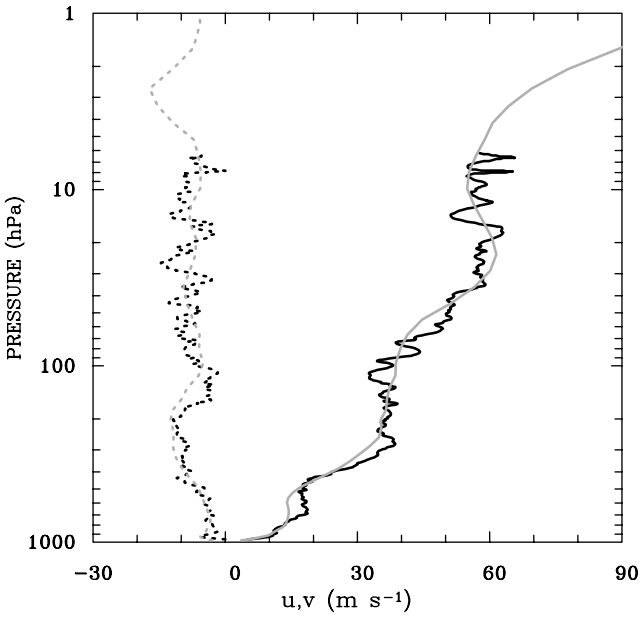

Figure 9. Zonal (solid) and meridional (dotted) horizontal wind components versus altitude. The smoother gray lines are from the ECMWF assimilation, and the black lines from the Marambio radiosonde.

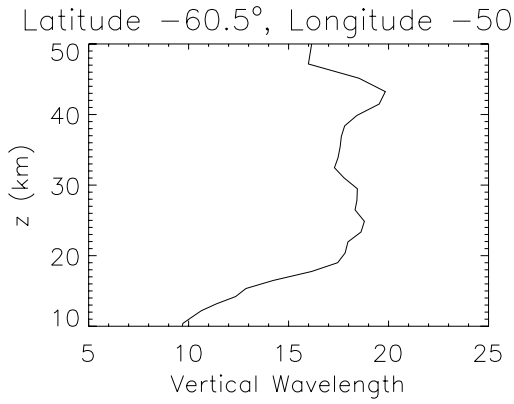

Figure 10. Mountain wave vertical wavelength (km) versus altitude using the dispersion relation and ECMWF winds in the direction of observed wave propagation.

westward, in the direction of wave propagation. The magnitude of this flux is similar to that observed for the large amplitude Andean mountain wave observed from CRISTA described by *Eckermann and Preusse* [1999] and *Preusse et al.* [2002].

5. Summary

[27] We present AIRS observations of a mountain wave event over the Antarctic Peninsula on 10 September 2003. We further use the observations to derive the 3-d properties of the wavefield. A wave feature with horizontal wavelength of 300 km, vertical wavelength of 20 km, and propagation direction 41° west of north is observed in the stratosphere above 30 km altitude. This event has long enough horizontal wavelength to appear in both AIRS radiance and temperature retrieval perturbations. We derive an estimate of the temperature amplitude of the wave from the radiance amplitude, corrected with the vertical wavelength-dependent attenuation factor derived by *Alexander and Barnet* [2007]. The 12 K result agrees with the wave temperature amplitude seen in the AIRS retrieved temperature field. This case study comparison suggests we may be able to use this procedure in other cases to derive wave temperature amplitudes directly from AIRS radiance measurements. Because AIRS radiances have three times better horizontal resolution than the retrieved temperatures, this will allow routine observation of gravity waves with horizontal wavelengths as short as 80 km, and estimates of wave momentum flux.

[28] We also found ECMWF assimilation and forecast wind and temperature fields to show a wave event with very similar properties. The 300-km horizontal wavelength is approximately 9 times the horizontal resolution of the ECMWF model. The wave is stationary in the ECMWF data, and present in the stratosphere for at least 24 h. The wave propagation is also approximately 180 degrees from the direction of the near-surface winds, and these winds in turn are approximately perpendicular to the orientation of the Antarctic peninsula topographic ridge. The wave is therefore identified as a mountain wave forced by flow over the peninsula topography. Analysis of radiosonde wind profiles near the center of the wave pattern also show a wave with the same propagation direction. The observed vertical wavelength is also consistent with the linear gravity wave dispersion relation for a stationary mountain wave propagating vertically through the ECMWF background wind field.

[29] Although the wave observed in the ECMWF fields has a horizontal wavelength only 9 times the horizontal resolution of the model, the comparison to the observations shows the model clearly represents the correct horizontal and vertical scales of the wave and its propagation direction, amplitude, and approximate timing.

[30] **Acknowledgments.** This work was supported by the NASA program Earth System Science Research using Data and Products from TERRA, AQUA, and ACRIM Satellites, grant NASA#NNH04CC54C. The authors thank Chris Barnet and Lars Hoffmann for valuable discussions about the radiative transfer of the AIRS measurements, and Steve Eckermann and Andreas Dörnbrack for their helpful comments on drafts of the manuscript.

References

Alexander, M. J., and C. Barnet (2007), Using satellite observations to constrain gravity wave parameterizations for global models, *J. Atmos. Sci.*, *64*, 1652–1665.

Aumann, H. H., D. Gregorich, S. Gaiser, D. Hagan, R. J. Pagano, L. Strow, and D. Ting (2000), AIRS algorithm theoretical basis document, level 1b, part 1: Infrared spectrometer, p. 70.

Aumann, H. H., et al. (2003), Airs/amsu/hsb on the aqua mission: Design, science objectives, data products, and processing systems, *IEEE Trans. Geosci. Remote Sens.*, *41*, 253–264.

Bacmeister, J. T. (1993), Mountain-wave drag in the stratosphere and mesosphere inferred from observed winds and a simple mountain-wave parameterization scheme, *J. Atmos. Sci.*, *50*, 377–399.

Bacmeister, J. T., P. A. Newman, B. L. Gary, and K. R. Chan (1994), An algorithm for forecasting mountain wave-related turbulence in the stratosphere, *Weather and Forecasting*, *9*, 241–253.

Bacmeister, J. T., M. R. Schoeberl, L. R. Lait, P. A. Newman, and B. Gary (1990), ER-2 mountain wave encounter over Antarctica: Evidence for blocking, *Geophys. Res. Lett.*, *17*, 81–84.

Carslaw, K. S., et al. (1998), Increased stratospheric ozone depletion due to mountain-induced atmospheric waves, *Nature*, *391*, 675–678.

Dörnbrack, A., M. Leutbecher, R. Kivi, and E. Kyro (1999), Mountain-wave-induced record low stratospheric temperatures above northern Scandinavia, *Tellus*, *51A*, 951–963.

Dörnbrack, A., M. Leutbecher, J. Reichardt, A. Behrendt, K. P. Müller, and G. Baumgarten (2001), Relevance of mountain wave cooling for the formation of polar stratospheric clouds over Scandinavia. Mesoscale dynamics and observations for January 1997, *J. Geophys. Res.*, *106*, 1569–1582.

Eckermann, S. D., and P. Preusse (1999), Global measurements of stratospheric mountain waves from space, *Science*, *286*, 1534–1537.

Eckermann, S. D., and D. L. Wu (2006), Imaging gravity waves in lower stratospheric AMSU-A radiances. Part 1: Simple forward model, *Atmos. Chem. Phys.*, *6*, 3325–3341.

Eckermann, S. D., A. Dörnbrack, S. Vosper, H. Flentje, M. J. Mahoney, T. P. Bui, and K. S. Carslaw (2006a), Mountain wave-induced polar stratospheric cloud forecasts for aircraft science flights during SOLVE/THESEO 2000, *Wea. Forecasting*, *21*, 42–68.

Eckermann, S. D., et al. (2006b), Imaging gravity waves in lower stratospheric AMSU-A radiances. Part 2: Validation case study, *Atmos. Chem. Phys.*, *6*, 3343–3362.

Ern, M., P. Preusse, M. J. Alexander, and C. D. Warner (2004), Absolute values of gravity wave momentum flux derived from satellite data, *J. Geophys. Res.*, *109*, D20103, doi:10.1029/2004JD004752.

Fritts, D. C., and M. J. Alexander (2003), A review of gravity wave dynamics and effects on the middle atmosphere, *Rev. Geophys.*, *41*(1), 1003, doi:10.1029/2001RG000106.

Fueglistaler, S., S. Buss, B. P. Luo, H. Wernli, H. Flentje, C. A. Hostetler, L. R. Poole, K. S. Carslaw, and T. Peter (2003), Detailed modeling of mountain wave PSCs, *Atmos. Chem. Phys.*, *3*, 697–712.

Höpfner, M., et al. (2006), Mipas detects Antarctic stratospheric belt of NAT PSCs caused by mountain waves, *Atmos. Chem. Phys.*, *6*, 1221–1230.

Jiang, J. H., D. L. Wu, and S. D. Eckermann (2002), Upper atmosphere research satellite (UARS) MLS observation of mountain waves over the Andes, *J. Geophys. Res.*, *107*(D20), 8273, doi:10.1029/2002JD002091.

Jiang, J. H., S. D. Eckermann, D. L. Wu, and J. Ma (2004), A search for mountain waves in MLS stratospheric limb radiances from the winter northern hemisphere: Data analysis and global mountain wave modeling, *J. Geophys. Res.*, *109*, D03107, doi:10.1029/2003JD003974.

McFarlane, N. A. (1987), The effect of orographically excited gravity wave drag on the general circulation of the lower stratosphere and troposphere, *J. Atmos. Sci.*, *44*, 1775–1800.

Palmer, T. N., G. J. Shutts, and R. Swinbank (1986), Alleviation of a systematic westerly bias in general circulation and numerical weather prediction models through an orographic gravity wave drag parameterization, *Q. J. R. Meteorol. Soc.*, *112*, 1001–1039.

Preusse, P., A. Dörnbrack, S. D. Eckermann, M. Riese, B. Schaeler, J. T. Bacmeister, D. Broutman, and K. U. Grossmann (2002), Space based measurements of stratospheric mountain waves by CRISTA 1. Sensitivity, analysis method and a case study, *J. Geophys. Res.*, *107*(D23), 8178, doi:10.1029/2001JD000699.

Susskind, J., C. C. Barnet, and J. M. Blaisdell (2003), Retrieval of atmospheric and surface parameters from AIRS/AMSU/HSB data in the presence of clouds, *IEEE Trans. Geosci. Remote Sens.*, *41*, 390–409.

Susskind, J., C. Barnet, J. Blaisdell, L. Iredell, F. Keita, L. Kouvaris, G. Molnar, and M. Chahine (2006), Accuracy of geophysical parameters derived from atmospheric infrared sounder/advanced microwave sounding unit as a function of fractional cloud cover, *J. Geophys. Res.*, *111*, D09S17, doi:10.1029/2005JD006272.

Tsuda, T., M. Nishida, C. Rocken, and R. H. Ware (2000), A global morphology of gravity wave activity in the stratosphere revealed by the GPS occultation data (GPS/MET), *J. Geophys. Res.*, *105*, 7257–7274.

Wu, D. L. (2004), Mesoscale gravity wave variances from AMSU-A radiances, *Geophys. Res. Lett.*, *31*, L12114, doi:10.1029/2004GL019562.

Wu, D. L., and J. G. Jiang (2002), MLS observation of gravity waves over Antarctica, *J. Geophys. Res.*, *107*(D24), 4773, doi:10.1029/2002JD002390.

M. J. Alexander, NorthWest Research Associates, Colorado Research Associates Div., 3380 Mitchell Lane, Boulder, CO 80301, USA. (alexand@cora.nwra.com)

H. Teitelbaum, Laboratoire de Meteorologie Dynamique, E.N.S. 24 rue Lhomond, 75235 Paris cedex 05, France.